Journal of Power Sources 196 (2011) 10806–10816

Contents lists available at SciVerse ScienceDirect

Journal of Power Sources

journal homepage: www.elsevier.com/locate/jpowsour

Surfactant directed self-assembly of size-tunable mesoporous titanium dioxide microspheres and their application in quasi-solid state dye-sensitized solar cells

Wei Chen [a,b], Yongcai Qiu [a], Keyou Yan [a], Shihe Yang [a,*]

[a] Department of Chemistry, The Hong Kong University of Science and Technology, Clear Water Bay, Kowloon, Hong Kong
[b] Michael Grätzel Centre for Mesoscopic Solar Cells, Wuhan National Laboratory for Optoelectronics and College of Optoelectronic Science and Engineering, Huazhong University of Science and Technology, Wuhan 430074, PR China

ARTICLE INFO

Article history:
Received 19 July 2011
Received in revised form 2 September 2011
Accepted 3 September 2011
Available online 10 September 2011

Keywords:
Size tunable
Titanium dioxide microsphere
Self-assembly
Dye-sensitized
Solar cell
Gel electrolyte

ABSTRACT

This paper provides mechanistic insight into the self-assembly involved in the controlled synthesis of mesoporous TiO_2 microspheres with tunable sizes (200 nm, 400 nm and 600 nm on average). The salient features of these microspheres, when used as building blocks of photoanode films in lieu of traditional small nanoparticles, have been systematically studied for the first time in highly viscous gel-electrolyte-based dye-sensitized solar cells. The light scattering property, electron transport and interface recombination kinetics have been critically compared with respect to the morphology and the size of the building blocks. A >6.78% power conversion efficiency was achieved with the 400 nm microspheres due to the balanced combination of light scattering, electrolyte permeation and charge collection advantages. This accentuates the performance limiting factor of the small nanoparticles and the 600 nm microsphere photoanodes as the difficulty for the quasi-solid electrolyte to fill in their long, narrow mesoscopic pore channels, a scenario supported by their short electron lifetimes as measured by intensity modulated photovoltage spectroscopy (IMVS).

1. Introduction

In recent years, there is a growing trend to integrate specialized nanostructures into dye-sensitized solar cells (DSSC), such as mesoporous microspheres with a submicrometer size [1–9], nanotube/nanowire arrays [10–13], *etc.*, in order to enhance light harvesting and charge collection, and to address new challenges in emerging applications and branching directions such as flexible [14] and solid-state DSSCs [15].

Submicrometer mesoporous microspheres are promising photoanode material alternatives to the traditional randomly assembled nanoparticles. The first advantage is the pre-formation of inter-particle connections inside the separated microspheres, a feature which is important for flexible DSSC applications [14]. Secondly, the microspheres possess a special hierarchical structure which can be tuned on at least two length scales. The primary building blocks, 10–20 nm nanoparticles comprising the microspheres, guarantee a high surface area for dye adsorption when used for assembling photoanodes. Secondary construction units of submicrometer microspheres provide the photoanode with a strong light scattering ability, potentially overcoming the intrinsic weak absorption of Ru-complex dye sensitizers in the near-infrared region [2,9]. Such a smart design simplifies the film fabrication process in comparison to the traditional photoanodes which employ, for example, a second large-particle layer on top of the nanoparticle underlayer to scatter back the near infra-red light. Encouragingly, recently reported efficiency has reached as high as more than 10% with only a single layer of TiO_2 microspheres [6]. Nevertheless, up to the present, little attention has been paid to the potential benefit of the sizable inter-microsphere cavities for quasi-solid state DSSCs (QS-DSSCs). Such inter-microsphere cavities may solve the pore-filling problem that has so far plagued researchers in developing QS-DSSCs and fully solid state DSSCs based on traditional nanoparticle photoanodes [16–18]. Besides, before the microspheres can be used as a new competitive photoanode material, the role of the inter-microsphere cavities, the contacts between the microspheres, and their size and morphology dependence need to be fully elucidated [19–21].

This paper seeks to address these issues. First, we carried out a series of comparative experiments to sort out the kinetic factors important in the self-assembly process for the morphology/size control and size focusing in the synthesis of the size-tunable TiO_2 microspheres. Second, such a microsphere size adjustability allowed us to clearly reveal, study and exploit the microsphere size effects in DSSCs, and thus optimize the cell performance. In particular, we have attempted to exploit the spacious inter-microsphere cavities for facilitating the accommodation and transport of a highly viscous (QS) electrolyte, validating the concept of using the micro-

* Corresponding author. Tel.: +852 23587362; fax: +852 23581594.
E-mail address: chsyang@ust.hk (S. Yang).

0378-7753/$ – see front matter © 2011 Elsevier B.V. All rights reserved.
doi:10.1016/j.jpowsour.2011.09.011

spheres for high-performance QS-DSSCs. The optimization study on the QS-DSSCs is expected to furnish guidelines for their future developments and set the stage for integrating the microspheres into all solid-state DSSC systems, meeting the grand challenge for the large-scale deployment of cheap, durable and environmental friendly DSSCs.

2. Experimental

2.1. Microspheres synthesis

A typical procedure with a normal sequence of adding reagents for the microspheres preparation is as follows. 1 g of tetra-n-butyl titanate ($Ti(nOBu)_4$) was added into a 45 ml ethanol solution of 1 g decylamine (DA). Into the resulting solution 15 ml of H_2O was then added dropwise under vigorous stirring. After continuous stirring for another 2 h, a white precipitate was formed, which was centrifugally collected, washed with excess ethanol, and kept for hydrothermal treatment and characterizations. For comparative studies, different amounts of metal source reagents, 0.5 g, 3 g $Ti(OBu)_4$, 0.84 g isopropyl titanate ($Ti(iOPr)_4$) and 0.89 g tetra-n-butyl zirconate ($Zr(nOBu)_4$), were used instead of 1 g $Ti(nOBu)_4$ in given preparation experiments, while the mole ratios of Ti(Zr) source: DA:H_2O remained the same. Experiments were also performed with a reverse sequence of adding the 15 ml of H_2O to a DA solution first, followed by a dropwise addition of the 15 ml ethanol solution of $Ti(nOBu)_4$. Hydrothermal treatment was carried out by a similar procedure reported previously [2]. After hydrothermal treatment, the resulting white precipitate was centrifugally collected and washed with excess ethanol.

2.2. Photoanode film fabrication

For viscous paste formation, 1 g of the powder product from the hydrothermal treatment was dispersed in 2.5 ml of H_2O, and 50 mg of PEO2000000 was added as a binder. After a homogenous paste was obtained by continuously magnetic stirring, it was spread onto a conductive glass substrate (fluorine tin oxide-coated glass, 14 Ω square^{-1}, Nippon Sheet Glass, Osaka, Japan) by the doctor blade technique. The film was then calcined at 450 °C for 30 min in air. After treatment in a 40 mM $TiCl_4$ aqueous solution at 70 °C for 10 min, the film was washed with distilled water and calcined again at 500 °C for 30 min. For the reference photoanode film preparation, a commercial nanoparticle paste purchased from JGC Catalysts and Chemicals Ltd., Kitakyushu-Shi, Japan (PASOL HPW-18NR) was used.

2.3. General material characterization

The morphologies were directly examined by using SEM using a JEOL 6700F at an accelerating voltage of 5 kV. For TEM observations, the samples were ultrasonically dispersed in ethanol and then dropped onto carbon-coated copper grids. The TEM experiments were carried out on JEOL 2010F and 2010 microscopes, both operating at 200 kV. Film thickness was measured with a Tencor Alpha-Step 200 surface profiler system. The film thickness was confirmed by three independent measurements. BET surface area was characterized using a Coulter SA 3100 surface area analyzer. For BET characterization of the as-prepared microsphere films, they were scratched, detached and collected from the conductive glass substrates. The XRD analyses were performed on a Philips PW-1830 X-ray diffractometer with Cu Kα radiation (λ = 1.5406).

2.4. Solar cell assembly and characterization

Films for solar cell tests were cut into a 5 mm × 5 mm beforehand. While still warm after being removed from the oven, the films were quickly immersed into a mixed acetonitrile/tert-butyl alcohol solution (1:1 in volume) containing 5×10^{-4} M N719 dye (cis-bis(isothiocyanato)bis(2,2′-bipyridyl-4,4′-dicarboxylato)-ruthenium(II) bis-tetrabutylammonium, Suzhou Chemsolarism, China) for 12 h. The dye-coated electrodes were then assembled into QS-DSSCs with a Pt sputtered FTO counter-electrode and a gel electrolyte containing 0.1 mol L^{-1} LiI, 0.1 mol L^{-1} I_2, 0.6 mol L^{-1} 1,2-dimethyl-3-propyl imidazolium iodide, 0.45 mol L^{-1} N-methylbenzimidazole, 10 wt.% PEO2000000 in 3-methoxypropionitrile. *J–V* characteristic curves were recorded using an IM6x electrochemical workstation. The light source (Oriel solar simulator, 450 W Xe lamp, AM 1.5 global filter) was calibrated to 1 sun (100 mW cm^{-2}) using an optical power meter (Newport, Model 1916-C) equipped with a Newport 818P thermopile detector. IPCE was measured based on a Jobin-Yvon Triax 190 monochromator. IMPS/IMVS were taken by the Zahner Zennium C-IMPS system with a green light-emitting diode (525 nm, LED).

3. Results and discussion

3.1. Size controlled synthesis

The two-step synthesis of mesoporous TiO_2 microspheres consists of the precursor preparation and the final hydrothermal fixing. It should be mentioned that Chen et al. [1] proposed a self-assembly mechanism for microsphere formation. By varying the long chain alkylamine content, they found the as-produced microspheres exhibiting different porosity, pointing to the role of the long chain alkylamine as the structural directing agent in mediating the microsphere formation. It is important to recognize that such synthesis involved reaction systems with low water contents (H_2O:Ti < 10), in which the hydrolysis of Ti source could be easily controlled. Similar low water content synthesis was reported in the literature for mesoporous TiO_2 microspheres [8]. In marked contrast, we adopted a high water content condition (H_2O:Ti ≈ 280) for the synthesis of mesoporous TiO_2 microspheres, with a view to facilitating hydrolysis of the Ti precursor so as to promote, in our opinion, the full crystallization of the mesoporous microspheres by eliminating any residual $-OCH_2CH_3$ (–OEt) groups in the following hydrothermal Oswald ripening process. As a consequence of using the high water content reaction system, kinetic control of the self-assembly process became more critical to obtain mesoporous spheres of a given size with a wormlike mesostructure, which nevertheless would provide the sensitivity needed to elucidate the formation mechanism of the mesoporous microspheres. Indeed, the classical LaMer model can be invoked to interpret our synthesis results as will be presented below [22,23].

Shown in Fig. 1 are SEM images of the precursors obtained under different reaction conditions. In general, they resultant products exhibit different morphologies (spheres and irregular particles), sizes (ranging from a few tens nanometers to several micrometers), size distributions and mesoscopic structural organizations. In particular, several points merit attention: (1) the microsphere size control depends on the source materials' concentration and their identity; (2) the product shape is related to the sequence of adding the source materials of $Ti(nOBu)_4$ and H_2O; and (3) the microsphere self-assembly process relies on the control over the reactivity of the inorganic source materials impinging on the products' mesoscopic structural organization.

The first point carries the importance of the Ti source concentration in effecting the size variation and size uniformity of the

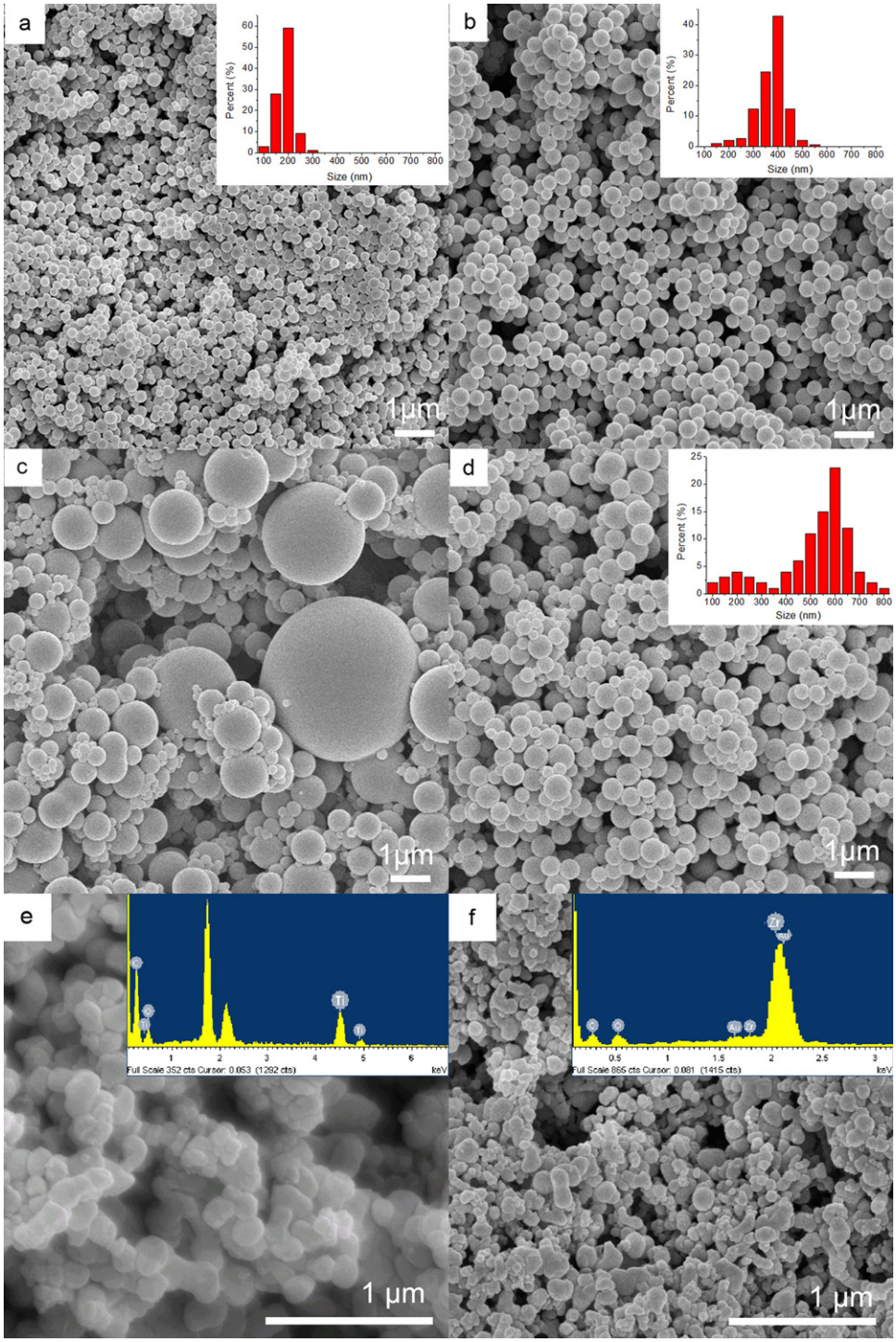

Fig. 1. (a–d) SEM images of mesoporous TiO_2 microspheres with tunable sizes, obtained by (a–c) varying the concentrations (from low to high) of the source materials ($Ti(nOBu)_4$:DA:H_2O = 1:1:15 by weight), and (d) changing the Ti source and solvent species. (e) SEM image of mesoporous TiO_2 particles with deformed shapes obtained under the same conditions as in (a–c), except for the reversed sequence of adding H_2O and $Ti(nOBu)_4$. (f) SEM image of ZrO_2 particles synthesized under the same conditions as in (a–c), except for the use of different Zr-source reagents. The insets in (a), (b) and (d) are size distributions of the corresponding microspheres. The insets in (e) and (f) are EDX results of the corresponding products.

resultant TiO_2 microspheres (Fig. 1a–c). As the amount of $Ti(nOBu)_4$ was increased from 0.5 g, 1.0 g to 3.0 g while keeping the ratio of DA:H_2O:Ti constant, the average size of the as-synthesized microspheres increased from 200 nm, 400 nm to uncontrollably over 1 μm.

During the synthesis of these three product samples, the reagents were added in the normal sequence. By first adding $Ti(nOBu)_4$ to the ethanol (EtOH) solution of DA, the $–NH_2$ groups are expected to attack the $Ti(OEt)_4$ oligomers resulting from alcoholysis, leading to the attachment of DA to the surfaces of the oligomers through postulated Ti–NH–bonds [24]. The resultant precursor is termed "hybrid chain" hereafter (Scheme 1). Indeed, the corresponding FTIR data support the formation of the Ti–NH–bonds (Fig. S1) with a characteristic –NH– wagging peak at 879 cm^{-1}, which is evidently shifted from the original value at 794 cm^{-1}. When H_2O was dropped into the system, hydrolysis first took place

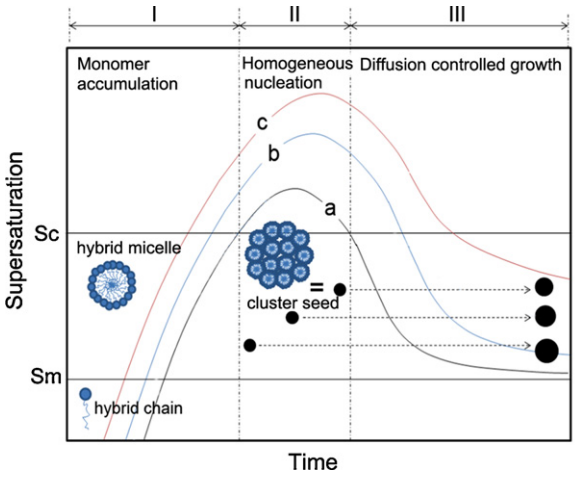

Scheme 1. Schematic showing the formation and size variation of the mesoporous TiO_2 microspheres in Fig. 1a–c. (a–c) Supersaturation profiles versus time, based on the LaMer model, corresponding to the conditions in Fig. 1a–c, respectively, with the source materials' concentrations changing from low to high. The microsphere growth is roughly divided into 3 periods separated by the vertical dashed lines (more appropriate for the case of curve a): "Period I" for monomer accumulation, wherein hybrid chains and micelles can be regarded as the monomers; "Period II" for homogenous nucleation, wherein clusters of a certain size are assembled from micelles; and "Period III" for diffusion controlled growth. S_c: critical supersaturation, the minimum supersaturation level for homogeneous nucleation of the smallest cluster seeds; S_m: critical supersaturation level for hybrid micelle formation.

at the hydrophilic end of the hybrid chain, resulting in Ti–OH bonds, which we believe could greatly strength the interaction between the hybrid chains. Hydrogen bond interaction and/or further condensation between the hydrophilic ends of the hybrid chains would lead to the formation of primary micelles; the critical micelle concentration of an organic surfactant (*e.g.*, DA) could be effectively reduced when the inorganic groups were added into the hybrid chains, in light of the cooperative self-assembly mechanism [25]. Driven by the decrease of the interfacial free energy in the reaction solution, the micelles would aggregate and yield organic–inorganic hybrid clusters with a suggested formula of $\{[TiO_x(OH)_y(OEt)_z(DA)_{4-2x-y-z}]_n\}_m$ (each chain has 1 Ti, each micelle has n chains, each cluster has m micelles) [26], which can be regarded as seeds for the growth of microspheres.

Following the LaMer model, we call the stage before micelle aggregation "the monomer accumulation period" (Period I in Scheme 1) and the stage after, "the homogeneous nucleation period" (Period II in Scheme 1). The separation between period I and II, which can be taken as the time point for the reaction solution to become light milk-white when a certain amount of H_2O was added. The color change reflects the micelle cluster seeds beginning to form. In the monomer accumulation period, isolated hybrid chain micelles are considered to have formed before they aggregated to stable seeds in solution. During this period, nucleation was not probable due to the low micelle concentration. Only aggregates of the micelles with a certain size can be regarded as critical nuclei capable of competing for the Ti source in the solution. Fig. 1a–c shows clearly that a lower micelle concentration (proportional to the amount of source materials added) yields a better size uniformity and smaller microspheres. As we know, the degree of supersaturation of the micelles should act as the driving force for the seed formation and therefore the microsphere growth [23]. A lower concentration, meaning a lower degree of supersaturation, would generate fewer hybrid cluster seeds of the microspheres in "the homogeneous nucleation period", and result in their slower growth in the following "diffusion controlled growth period". With further dropwise addition of H_2O and vigorous stirring of the solution, the hybrid chains and/or the newly formed micelles (the monomer of Ti source) would decrease in concentration to the extent that nucleation would stop, entering "the diffusion controlled growth period" (Period III in Scheme 1). These micelles would then diffuse onto the surface of the cluster seeds, fueling the continuous growth of the microspheres. In this period, the particle growth rate is inversely proportional to the particle size, meaning that smaller seeds grow faster and larger seeds grow slower, *i.e.*, size focusing of the particles occurs [27]. As a result, the as-produced TiO_2 microspheres tend to reach uniform size, as is the case in Fig. 1a and b. When the concentration of hybrid micelles was too high, the growth would be too fast so that the particle size focusing effect ceased to be effective, yielding microspheres with a uncontrolled size distribution, just as the situation shown in Fig. 1c: the size of large microspheres has reached up to 4 μm whereas the smallest ones in the same sample are only about 100 nm in diameter.

According to the LaMer model widely employed to explain particle growth kinetics [22], we illustrate in Scheme 1 the relationship of supersaturation of micelles versus time when H_2O was dropwisely added under stirring to reaction systems of different starting Ti source concentrations. Curves a, b and c correspond to samples in Fig. 1a, b and c, respectively. Due to the higher supersaturation of the sample in Fig. 1c, a shorter monomer accumulation time and a longer homogenous nucleation time are expected, as can be seen from curve c when compared to curves a and b. Bearing in mind that the cluster seeds born at a earlier moment of the nucleation period should have a longer growth history than those of the seeds born later on, a broader nucleation period (curve c versus curves b and a) should yield a wider size distribution of the products, as revealed by comparison of Fig. 1c with Fig. 1b and a.

Second, when the Ti source and solvent were changed, respectively, to $Ti(iOPr)_4$ and isopropanol but with the same concentrations as those in Fig. 1b, the mean size of the as-produced microspheres increased to 600 nm, 200 nm larger than that in Fig. 1b, and the size distribution is also relatively wider, as shown in Fig. 1d. This mostly arises from the fact that $Ti(iOPr)_4$ with the less electrophilic–iOPr groups is more reactive towards H_2O than $Ti(OEt)_4$ [26]. Consequently, the hydrolysis and condensation would be faster, leading to faster micelle formation (monomer accumulation), micelle assembly into be bigger cluster seeds (nucleation), and the microsphere growth. This is analogous to the high supersaturation case in Scheme 1, hence accounting for the wider size distribution and larger average size of the microspheres in Fig. 1d than in Fig. 1b.

Third, when the sequence of adding reagents was reversed, *i.e.*, H_2O was added to DA solution before the dropwise addition of ethanol solution of $Ti(nOBu)_4$, we obtained the product particles in Fig. 1e, which look more irregular in shape and smaller in size than those in Fig. 1b, notwithstanding the same source material concentrations. This seems to evidence the critical importance of the DA modified hybrid chains in the self-assembly process of microspheres. It is a common experience that the synthesis of uniform spherical TiO_2 particles is much harder than that of spherical SiO_2 particles chiefly because the transition metal ions are generally more electrophilic and more liable to increase the coordination number [26]. A typical strategy has been to modify the Ti precursors by adding salts for electrostatic stabilization or polymeric stabilizers such as hydroxypropyl cellulose and block copolymers [28]. In a similar vein, the DA we used here for the synthesis of TiO_2 microspheres serves an important stabilization function: its long alkyl tail prevents the Ti center from fast hydrolysis.

In the normal addition sequence of Ti source and H_2O, $Ti(nOBu)_4$ was initially dissolved in ethanol solution of DA and there was sufficient time for alcoholysis of the Ti source and DA coordination reaction in the solution to form the Ti–NH–bond. So the DA modified hybrid chains were allowed to form before their hydrol-

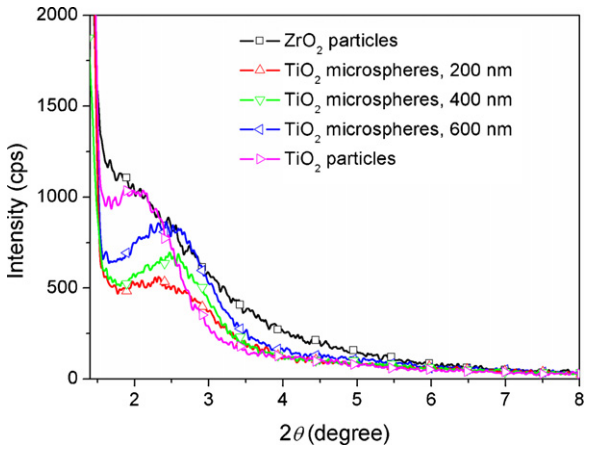

Fig. 2. Small angle XRD patterns of hybrid samples which are shown in Fig. 1.

ysis. In the reverse addition sequence, however, when $Ti(nOBu)_4$ was added dropwise to the H_2O and DA containing ethanol solution, both H_2O and DA would competitively react with the Ti source, which could disturb the formation of DA modified hybrid chains and thus the subsequent cooperative self-assembly process. If the hydrolysis and condensation reactions of the Ti source took place very rapidly, the inorganic ends of the hybrid micelles would be inevitably too large, hence they disturb the normal self-assembly process and produce particles of irregular shape. Moreover, uncontrolled hydrolysis of the Ti source, meaning excessively high supersaturation of the reaction system, would yield an overflow of cluster seeds during the homogenous nucleation period and beyond. The excessive seeds would all compete for the Ti source (monomer) in the reaction solution, would result in particles of much smaller sizes.

Finally, when $Zr(OBu^n)_4$ was used as the metal source reagent under otherwise identical conditions to those in Fig. 1b, the as-produced ZrO_2 hydrolysate (Fig. 1f) had a smaller size and more irregular shape. From this observation for the hydrolysis and condensation in the Zr source based reaction system, one finds that control has been lost. This is associated with the nature of the Zr center, which is more reactive towards H_2O than Ti counterparts, owing to its higher degree of coordination unsaturation [26]. Taken together from the above comparison study in the context of the LaMer model, the controllable hydrolysis and condensation are critical for the formation of the mesoporous hierarchical TiO_2 microspheres.

Fig. 2 shows small angle XRD patterns of the samples in Fig. 1. The sharpness of the peak reflects the degree of order in the mesostructure of the hybrid hydrolysates. For the 200 nm, 400 nm and 600 nm microspheres shown in Fig. 1a, b and d, evident Bragg peaks can be found at around 2.5°. According to the Bragg equation we can estimate the d-spacing of the repeating units to be about 3.5 nm, which is close to the reported size of the well known MCM-41 mesoporous material obtained by employing cetyltrimethyl ammonium bromide (CTAB) as the surfactant [29]. CTAB possesses similar alkyl chain length to DA, and the alkyl chain tends to huddle up in polar solvent [30], so their micelle sizes are thought to be similar and accordingly their templated mesostructure units are also similar in size. For the hybrid particles obtained by the reversed addition sequence of H_2O and Ti source shown in Fig. 1e, a peak, although weaker, centered at around 2.1° can also be detected. The XRD peak shift to a smaller angle implies that the repeating units in the mesostructure of the sample in Fig. 1e becoming relatively larger (about 4.2 nm). On the other hand, the weaker XRD peak of the sample in Fig. 1e demonstrates the short range order of the mesoporous structure, in reference to the previous analysis, *i.e.*, the hydrolysis and condensation of the Ti source have run out of control due to the reverse addition sequence of H_2O and Ti source. The observation of the mesoporous structure in the irregular particles in Fig. 1e indicates that the hybrid micelles still existed to a certain extent and performed the function of directing the self-assembly process, although the as-synthesized hydrolysate is somewhat deformed. Due to loss of control on the reaction of Zr center towards H_2O, the as-prepared Zr based hydrolysate has a short range order in its mesoporous structure, which is consistent with its small angle XRD pattern, of which no peak can be found.

Shown in Fig. 3 are TEM images of mesoporous TiO_2 microspheres obtained after hydrothermal treatment and direct high temperature calcination of the precursor microspheres shown in Fig. 1. These images clearly reveal the necessity of a suitable hydrothermal procedure to make the size tunable microspheres well crystallized (see high magnification TEM images in Fig. S2 for single crystallinity of each particle) and at the same time maintain appropriate porosity inside the microspheres. For the precursor microspheres shown in Fig. 1a, b and d, after hydrothermal treatment, their smooth surfaces became roughened due to embedment of nanocrystals. The sizes of the nanocrystals are about 10–20 nm and the pore sizes resulting from the assembly of these nanocrystals have comparable sizes to those of the building block nanocrystals, also about 10–20 nm. This size range just fits the requirements for DSSC photoanode materials [31]. Although direct calcination without hydrothermal treatment also yielded polycrystalline TiO_2 microspheres (Fig. 3d), the pore channels shrank evidently as revealed in its high magnification TEM image (the inset in Fig. 3d), which is direct testimony to the necessity of hydrothermal post treatment. Pore size distributions measured by the N_2 adsorption–desorption method (Fig. S3) also revealed the pore channel shrinking from 16 nm for the three kinds of hydrothermally treated microspheres to <3 nm for the directly calcined microspheres. It follows that the measured BET surface areas of the 200 nm, 400 nm and 600 nm mesoporous microspheres are nearly the same at around 120 $m^2\,g^{-1}$, whereas that for the directly calcined microspheres is only 15 $m^2\,g^{-1}$. Such pore shrinking arising from high temperature calcination commonly occurs in the surfactant directed self-assembly of mesoporous materials [32], simply because the surfactant micelles are too small (only 3 nm in our case here) to construct sufficiently strong pore walls to survive the crystallization process involving the rearrangement of Ti–O–Ti network in amorphous TiO_2 [33]. Powder XRD measurements confirmed that the nanocrystals in the three hydrothermally treated samples were all in anatase phase with sizes of 14–16 nm, with no causal relationship with the size of microspheres (Fig. S4).

3.2. Film fabrication and characterization for QS-DSSC

In order to study the size effect of the TiO_2 microspheres on the performance of QS-DSSCs, we used the three different sized microspheres to fabricate photoanode films. Shown in Fig. 4 are SEM images of the films made of 200 nm (Fig. 4a), 400 nm (Fig. 4b), 600 nm (Fig. 4c) mesoporous TiO_2 microspheres and the commercial nanoparticle film was used for reference (Fig. 4d). First of all, it is clear that the bigger the building blocks are, in the sequence from the nanoparticles, 200 nm microspheres, 400 nm microspheres to 600 nm microspheres, the larger cavities are formed in the films. From the insets of the four images, the cavities appear to be comparable in size to the building blocks. For microspheres based films, there is a second level of pores, *viz.*, the interstitials between the microspheres, in addition to the first level of mesopores inside the microspheres themselves. Such a hierarchical pore structure is thought to be of great benefit to electrolyte penetration. On the other hand, the nanoparticles reference film contains only nanosized pore channels. This pore size/structure difference may hold

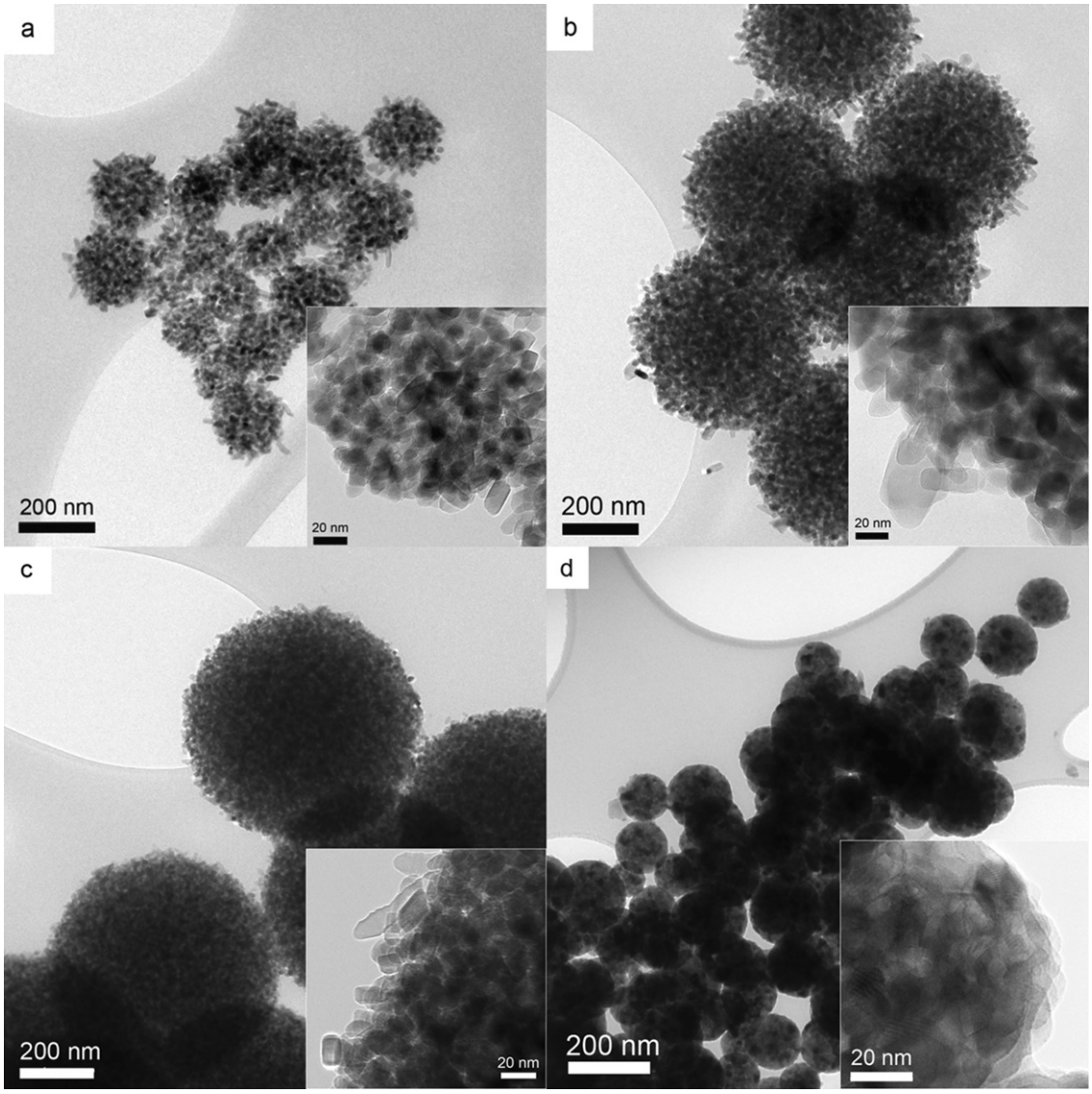

Fig. 3. TEM images of mesoporous TiO_2 microspheres with average size of (a) 200 nm, (b) 400 nm, and (c) 600 nm synthesized by hydrothermal treatment and direct calcination (d). The insets are the corresponding high magnification images.

the key in explaining their DSSC performance differences, as will be demonstrated in order below.

Besides their pore size difference, the ways in which the pores are connected may also be different between the nanoparticle- and microsphere-based films. For microsphere-based films, the inter-microsphere connections at their junctions were built up in the high temperature calcination procedure, while the connections between nanoparticles inside the microspheres were mostly formed in the hydrothermal procedure. On the other hand, the inter-nanoparticle connections in nanoparticle-based films were made during the calcination process through mass diffusion. Consequently, the linkage between the TiO_2 building blocks would be different. For example, the density of adhesive contacts between the building blocks inside the films plays an important role to maintain the morphological integrity against the accumulated stress during the heating process. This explains why increasing micrometer-level cracks appeared in the films with the increasing size of the building blocks, from the nanoparticles (Fig. 4d) to the 200 nm (Fig. 4a), 400 nm (Fig. 4b) and 600 nm (Fig. 4c) microspheres. This would influence the electron transport kinetics as will be discussed below together with intensity modulated photocurrent spectroscopy (IMPS) results.

Diffuse reflectance spectroscopy can reveal the light scattering capability of the photoanode films [2]. Strong light scattering increases the effective optical length of the film, contributing to the enhanced light harvesting in the 600–750 nm wavelength region for high performance DSSCs. Only when the particle size in the film is comparable to the visible light wavelength (>400 nm) will the light scattering be strong in the visible vision in accordance with the Mie theory [34,35]. Unfortunately, large particles inevitably fall short of the surface area needed to adsorb a sufficient amount of dye molecules. A way out is to design a double-layered photoanode film, namely, a small nanoparticle underlayer overlaid by a large-particle light-scattering top layer [36]. Even simpler is the use of mesoporous microspheres with an inherently hierarchical structure, for which a single layer film can fulfill the dual demands of dye adsorption and light scattering.

Shown in Fig. 5 are diffuse reflectance spectra of size-tunable microsphere-based films and the reference nanoparticle film. A common feature is a steep increase in reflection in the wavelength region ranging from 350 to 400 nm, caused by the intrinsic band gap absorption of TiO_2. The light reflection in the visible wavelength region is associated with the scattering events when photons transfer through the films; a higher intensity reflects a higher light

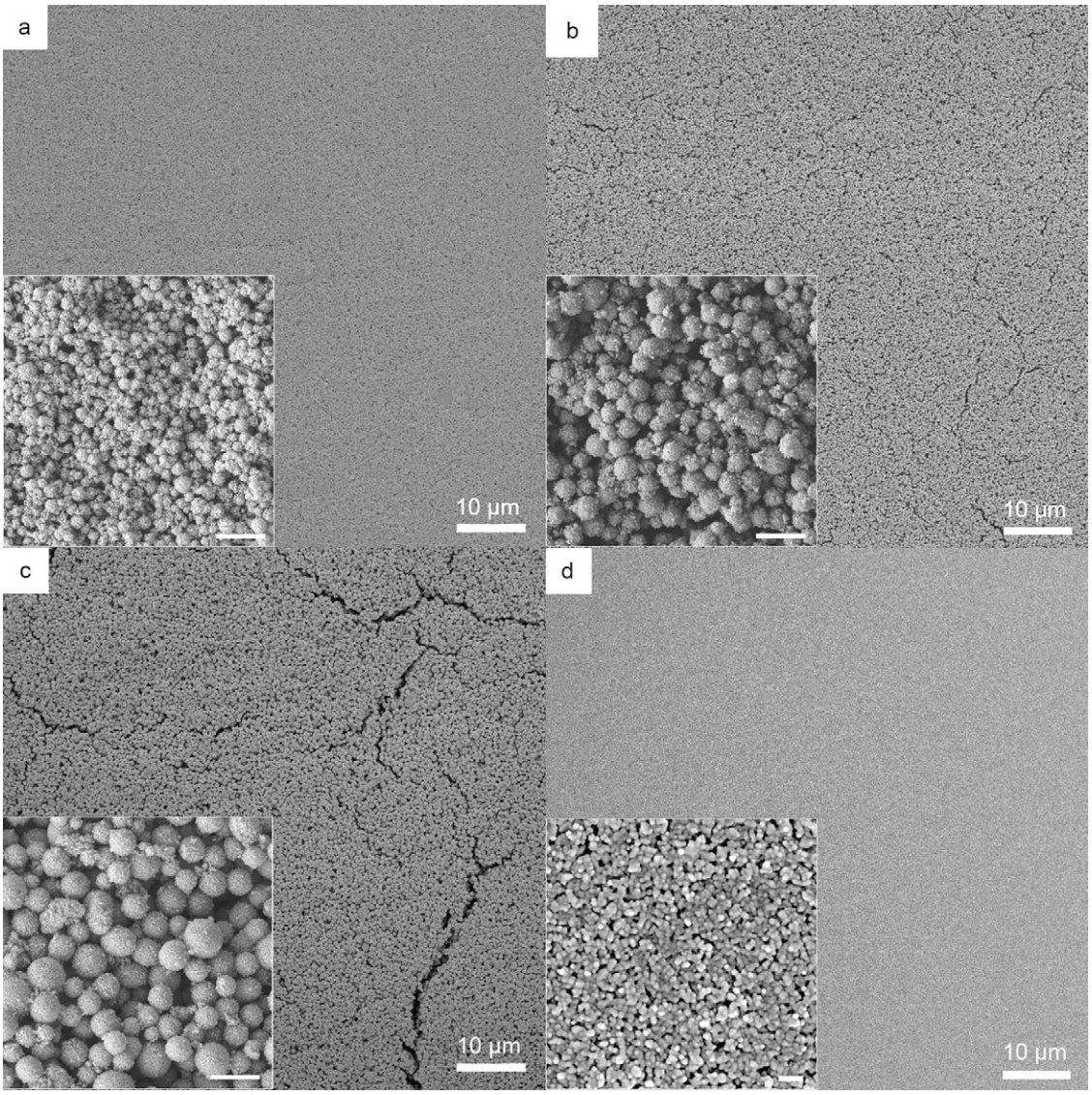

Fig. 4. SEM images of films made of mesoporous TiO_2 microspheres with an average size of (a) 200 nm, (b) 400 nm, (c) 600 nm and made of (d) commercial TiO_2 nanoparticles, with nearly the same thickness of about 10 μm. Insets are high magnification images of the corresponding films with scale bars of (a–c) 1 μm and (d) 100 nm.

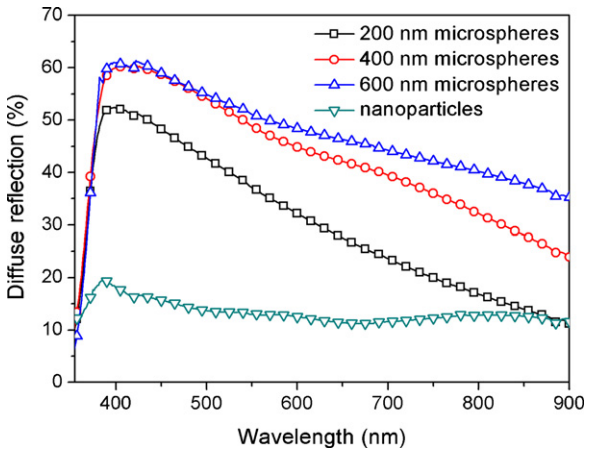

Fig. 5. Diffuse reflectance spectra of the TiO_2 films prepared from microspheres with different average sizes and the commercial nanoparticles. The film thicknesses are kept nearly the same at 10 μm.

scattering capability of the film material. Clearly, light scattering in the reference nanoparticle film is lowest among all of the four films in the spectral region of interest. Indeed, this film is optically transparent since closely-packed small nanoparticles make the film uniform at the length scale of visible wavelengths. The 200 nm microsphere film, however, looks optically translucent due to enhanced light scattering, giving rise to a reflectance ~10–20% higher than the nanoparticle film in the visible range. Increasing the microsphere size to 400 nm and 600 nm made the corresponding films opaque thanks to the even stronger light scattering of these microspheres. In detail, these two films made of the 400 nm and 600 nm microspheres display little reflectance difference in the relatively short wavelength range of 400–500 nm, while large reflectance differences gradually develop at around 600–750 nm, implying that further increase in the microsphere size to > 400 nm is less effective for light scattering enhancement, other than just extending the scattering peak towards a longer wavelength [35]. In short, we can conclude from the above: (1) the size increase from 18 nm of the commercial nanoparticles to 200 nm and then to 400 nm of the microspheres results in significant light scattering enhancement; and (2) further size increase from 400 nm to

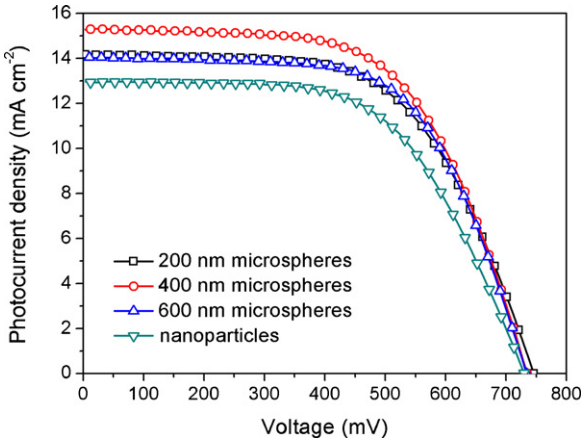

Fig. 6. *J–V* characteristic curves of the QS-DSSCs based on different mesoporous microspheres and commercial nanoparticles with their thicknesses optimized independently, as summarized in Table 1.

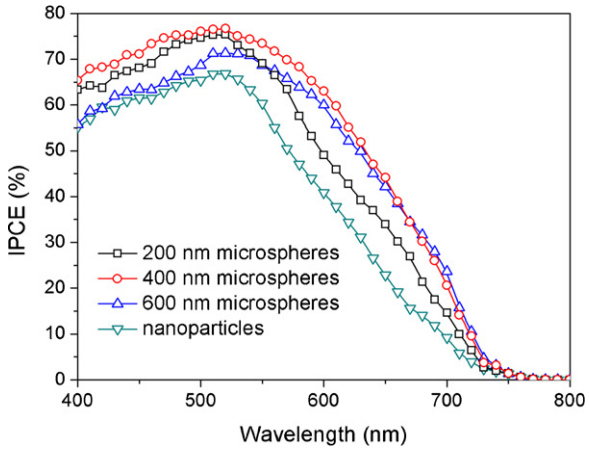

Fig. 7. IPCE spectra of the QS-DSSCs based on the mesoporous TiO_2 microspheres and commercial nanoparticles with their film thicknesses optimized independently, corresponding to the best performing cells listed in Table 1.

600 nm microspheres is less effective in enhancing the light scattering enhancement.

3.3. Performance test of the QS-DSSCs

The high surface areas of the mesoporous TiO_2 microspheres and the excellent light scattering ability of their films established above are desirable characteristics for QS-DSSCs. Fig. 6 shows photocurrent density–voltage (*J–V*) characteristic curves of the representative cells composed of different sized mesoporous TiO_2 microspheres and the reference nanoparticles, based on a quasi-solid state electrolyte using PEO2000000 as the gelator and measured at 1-sun equivalent light intensity. The measured parameters are listed in detail in Table 1. The cell performance for the photoanodes was optimized with respect to their film thicknesses. The dependences of short-circuit photocurrent density (J_{sc}) on the film thickness for the corresponding four solar cells follow a similar trend: their J_{sc} firstly increase, then saturate and then decrease (Fig. S5). The saturated J_{sc} was reached at different thicknesses for the four cells, mostly determined by different packing densities of TiO_2 nanoparticles in them. A higher packing density means a higher roughness factor per thickness and a shorter light extinction length of a given photoanode film. It follows that the reference nanoparticle film should have the highest packing density, while for the microspheres, the smaller their size, the higher their packing density in the films, in reference to their SEM images in Fig. 4.

The best performing cell with 6.78% efficiency is found to be the one made of the 400 nm microspheres owing primarily to its highest J_{sc} among all the four cells tested. This record efficiency is about 20% higher than that of the TiO_2 nanoparticles based DSSC reported previously [37], using an optimized PEO2000000 based gel electrolyte. In this comparative study under the same test conditions, the measured cell performance of the microsphere-based photoanodes is all significantly higher than that of the nanoparticles based photoanode, underscoring the superiority of the microspheres over the nanoparticles, especially in the highly viscous gel-electrolyte-based DSSC system. Among the three different sized microspheres, the best performing was found to be the intermediate-sized, which will be further discussed below together with the results of IPCE and IMPS/IMVS measurements.

It is encouraging that the efficiencies of our tested cells are in the high end among the QS-DSSCs reported to date [38–40]. In comparison to the recently reported liquid DSSC (efficiency > 10%) made of mesoporous TiO_2 microspheres [6], the biggest performance loss of our cells is in the relatively low fill factor (*FF*, ~0.60 versus 0.76) and low J_{sc} (15.3 mA cm^{-2} versus 18.2 mA cm^{-2}). Considering that much of the low *FF* and low J_{sc} of our QS-DSSCs can be attributed to the large sheet resistance and low transmittance of the FTO glass we used, the performance of our QS-DSSCs is indeed outstanding. Especially, the stability of our gel-electrolyte-based DSSCs is quite good: even without sealing, the cell performance only degrades by less than 15% after 6 days (Fig. S6). This is due to the gelation effect of PEO2000000 on the liquid electrolyte precursor, leading to a significant viscosity increase of the electrolyte so that the evaporation of volatile solvent (methoxypropionitrile) in it is minimized.

3.4. Mechanistic studies of the QS-DSSCs

We have shown above that the better cell performance with the 400 nm microspheres than with others is dominated by the maximum J_{sc} contribution. To sort out the contributions to the J_{sc} enhancement, we recorded IPCE spectra of the corresponding photoanode films [41], which are presented in Fig. 7. In sum, the 400 nm microsphere film appears to make the most of the photons absorbed by the N719 dye, in keeping with the highest J_{sc} obtained with this cell among all the four cells tested. The IPCE reaches a maximum of 76.6% at 520 nm, pointing to a nearly quantitative conversion of the incident photons to electric current when the light loss due to the FTO glass (~84% transmittance at 520 nm) is taken into account. This indicates that charge collection is not a limiting factor for the 400 nm microsphere-based cell with the gel electrolyte. The 200 nm microsphere film shares a similar situation in terms of charge collection (Table 1), but due to its less effective light harvesting and thus a lower IPCE in the 600–750 nm regions, the J_{sc} is lower. For the nanoparticle film and the 600 nm microsphere film, the maximum IPCE values (Table 1) are evidently lower than those of the other two films, alluding to the charge collection limitation. If so, the similar IPCE for the 600 nm microsphere film to that for the 400 nm microsphere film in the 600–750 nm region can only be ascribed to the higher light harvesting ability of the 600 nm microspheres arising from their strongest light scattering [41]. This is consistent with their diffuse reflection spectra shown in Fig. 5.

More direct information on charge collection of the cells under study was obtained from IMPS/IMVS measurements. For these measurements, the thicknesses of the film samples were similarly set at about 5 μm, which is shorter than the full extinction depth of light at 525 nm. The results are shown in Fig. 8. The observed power law dependence of electron transport time (τ_t) and recombination time (τ_r) on short-circuit photocurrent (J_{sc}) is in accordance with the well-known trapping–detrapping model describing elec-

Table 1
Cell parameters of the best performing QS-DSSCs with photoanodes made of different building blocks.

Samples	Light scattering	Thickness (μm)	$IPCE_{max}$ (%)	η_{cc}	V_{oc} (mV)	J_{sc} (mA cm^{-2})	*FF*	η (%)
200 nm MS	Moderate	7.2	75.4	0.87–0.88	746	14.2	0.60	6.32
400 nm MS	Strong	10.6	76.6	0.88–0.90	735	15.3	0.60	6.78
600 nm MS	Strongest	12.3	71.3	0.78–0.80	734	14.0	0.63	6.45
Nanoparticles	Low	13.3	66.8	0.68–0.73	730	13.0	0.59	5.62

MS, microspheres; η_{cc}, charge collection efficiency of films with thickness of ~5 μm.

tron diffusion in a DSSC [42,43]. The small variations of the slopes of the curves for the cells can be ascribed to different average coordination numbers of the TiO_2 nanoparticles in the four photoanode films as revealed by Frank et al. [42,43]: a higher coordination number corresponds to less sensitive dependence of τ_t (also τ_r) on light intensity I_0 (notice that $J_{sc} \propto I_0$). Indeed, the reference nanoparticle film has the highest packing density of nanoparticles (see SEM images in Fig. 4), and therefore possesses the highest coordination number, which explains why it has the smallest slope (the absolute value) of τ_t dependence on J_{sc}. The large-microsphere-based films, however, due to the submicrometer pores between the microspheres, clearly have a lower coordination number, hence a larger slope (the absolute value) of τ_t dependence on J_{sc}. On the basis of the above analysis, we believe that the tested IMPS/IMVS results are sound.

Several remarks need be made about Fig. 8. Firstly, according to the expression for charge collection efficiency, $\eta_{cc} = 1 - \tau_t/\tau_r$ [41–43], the largest gap between τ_t and τ_r observed for the 400 nm microsphere film reflects the best charge collection property of this film (η_{cc} = ~0.88–0.90 at different J_{sc} values). Similarly, η_{cc} for the 200 nm microsphere film is between 0.87and 0.88, confirming the inference above from the IPCE data. Due to the apparently shorter τ_r, η_{cc} for the 600 nm microsphere film is decreased to between 0.78 and 0.80 and that for the reference nanoparticle film to even smaller values of 0.68–0.73. The trend of varying charge collection depending on the building blocks for the four test films is consistent with their IPCE maxima: a larger η_{cc} corresponds to a higher $IPCE_{max}$ (see Table 1).

Secondly, it is interesting to find that τ_t appears to be less sensitive to the film morphologies than τ_r. The insensitivity of τ_t to film morphology is counter to the result of Kim et al. [8], who found that a commercial nanoparticle film possess similar τ_t to that of a distorted mesoporous TiO_2 microspheres film but much shorter τ_t than that of a well-defined mesoporous TiO_2 microspheres film. Kim et al. explained their result in terms of electron transport

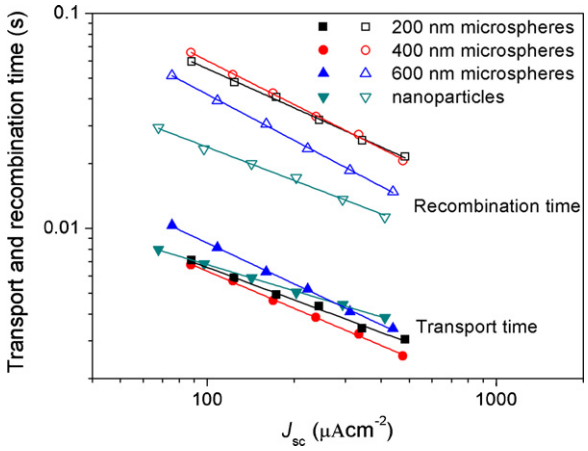

Fig. 8. Dependence of electron transport and recombination time on J_{sc} for QS-DSSCs based on the mesoporous TiO_2 microspheres and commercial nanoparticles under the illumination with a 525 nm diode.

hindrance at the inter-microsphere junctions. The electron transport hindrance would be high in well-defined microsphere films but low in distorted microsphere films owing to the larger necking area at the inter-microspheres junctions of the latter which can facilitate electron transport. Conceivably, the surface roughness of their microspheres and ours might be different due to the different hydrothermal treatment conditions: we used ammonia to promote crystallization instead of the neutral solution they used. Consequently, the surface of our microspheres contained many rod-like nanoparticles (*i.e.*, it was rougher, see Figs. 3 and 4) whereas the microspheres of Kim et al. mostly consist of only small cube-like nanoparticles, giving a smooth surface. This may explain why our microspheres tended to attach to each other. It follows that the problem of inter-microspheres electron transport hindrance is much less serious in our films. In fact, Sauvage et al. also showed by impedance measurement that their microspheres synthesized under similar hydrothermal conditions to ours exhibited a comparable electron diffusion coefficient (associated with electron transport rate) to that of a P25 nanoparticle film [6].

With reference to the best electron transport property for the 400 nm microsphere film, we suggest two possible explanations: (1) close packing of grains and crystal intergrowth within the microspheres may facilitate fast electron transport, a salient feature not shared by the reference nanoparticle film, as partially reflected in the low temperature treatment case [14]; (2) the pore structure of the 400 nm microsphere film may be best suited for the gel electrolyte penetration, which would enhance the Li^+ cations' specific adsorption on TiO_2 surface and diffusion. As suggested by Shi et al. [37], the well known ambipolar diffusion model [20], which was introduced to interpret the effect of cations on electron transport, is also valid in PEO2000000 gel-electrolyte-based DSSCs. Since fast Li^+ diffusion is a key ingredient in this model for assisting electron transport, we suggest that the pore structure plays an important role here to tune the electron transport rate in our four films tested.

For the sharply different τ_r caused by varied film morphologies, we have a special case for highly viscous gel-electrolyte-based DSSCs, which is not likely to happen for liquid electrolyte, but is very common for solid electrolytes, such as OMeTAD [17], or CuI, CuSCN [16]. Namely, it is associated with the pore filling problem depending on the pore structure in photoanode films. Sauvage et al. [6] once found a longer recombination time for a microsphere-based film than for a P25 nanoparticle film with liquid electrolyte, which was ascribed to the close packing of grains and crystal intergrowth within the microspheres. While this reasoning could apply to our QS-DSSCs as well, other possible reasons also need be considered because of the following. First, the reference nanoparticles paste we employed has been sufficiently optimized by the producer, as reflected from the high film quality (see SEM image in Fig. 4d). The as-produced film has achieved good J_{sc} record in liquid electrolyte based DSSCs, generally much better than P25 nanoparticle film [8]. So, its charge collection property is considered to be much better than that of P25 nanoparticle film. While Sauvage et al. [6] ascribed the shortening of recombination time in the P25 nanoparticle film in a liquid electrolyte to the insufficient inter-nanoparticles connection, we believe that the inter-nanoparticles connection in our reference film should be reasonably good. It is thus surprising to

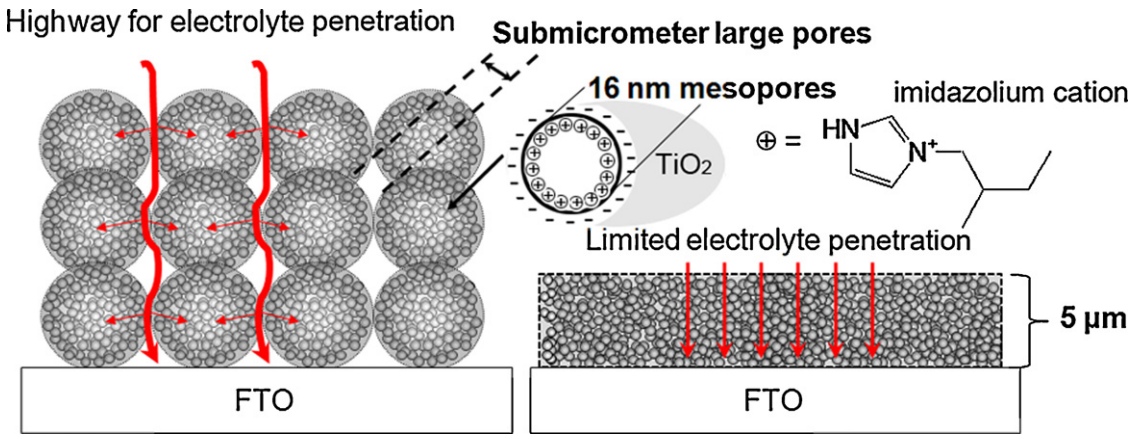

Scheme 2. Schematic illustration of pore structures and electrolyte penetration into these structures. Left, a mesoporous microsphere film; right, a nanoparticle film. The bold red lines highlight the highway for gel electrolyte penetration through the submicrometer pores between the microspheres, while the thin red lines from the surfaces to the core regions of the microspheres and from the top surface to the underlayer across the nanoparticle film highlight the narrow pore channel limited diffusion of the gel electrolyte. (For interpretation of the references to color in this scheme legend, the reader is referred to the web version of this article.)

find from Fig. 8 that τ_r for our reference nanoparticle film is also about two times shorter than that for the 400 nm microsphere film. This compelled us to propose a new model, which will be discussed below, for our special case with a highly viscous gel electrolyte instead of a liquid electrolyte. Second, the argument of close-packing and crystal intergrowth by Sauvage et al. [6] also cannot explain why in our case, the 600 nm microsphere film possesses an evidently shorter τ_r than the smaller microsphere films given that larger microspheres would give rise to more extensive close-packing and crystal intergrowth.

To reconcile these observations, we propose a new pore structure limited penetration mechanism as illustrated in Scheme 2. In comparison to the densely packed nanoparticle film, in which the gel electrolyte penetration is hindered by the narrow and long pore channels across the film thickness of 5 μm, the microspheres films possess much larger interstitial pores on the submicrometer scale. Such large pores can allow full electrolyte permeation and relatively free diffusion of ionic species, especially for imidazolium cations with a large molecular radius, and thus essentially act as a short-cut highway for the gel electrolyte. Moreover, establishment of an electrostatic double layer associated with ionic specific absorption would be much easier at the semiconductor/gel electrolyte contacts in the microsphere films than in the traditional mesoscopic particulate films, due to the more facile ion diffusion in the former. Such an electrostatic double layer has been suggested previously for ionic liquids of 4-tert-butyl-pyridine [44] and imidazole [45], the adsorption of which on TiO_2 surface was found to prolong the recombination time. For microspheres smaller than 400 nm, this positive effect of the hierarchical pores seems to be at play to the fullest in prolonging the recombination time. Further increase of the microsphere size to 600 nm (even 800 nm for some microspheres), however, would increase the difficulty of electrolyte penetration from outer surface to the core region of the microspheres through its mesopore channels (16 nm only in size, Fig. S3) and thus may begin to perpetuate negative effects, leading to shorter recombination times than those for smaller microspheres.

4. Conclusion

By using a kinetically controllable, surfactant-directed self-assembly strategy, alongside the subsequent hydrothermal treatment, we have successfully achieved size control of mesoporous TiO_2 microspheres in the range of 200–600 nm. Key to the microspheres synthesis is to control hydrolysis/condensation rates of the Ti source by the formation of DA modified hybrid chains, which allow the formation of hybrid micelles *via* kinetic control and their subsequent self-assembly into the microspheres. Our successful control over the microsphere size has allowed us to conduct the comparative study on the use of these microspheres in QS-DSSCs. Demonstrated are the high surface area provided by the inherent pores, efficient light harvest by the microsphere-enhanced light scattering, and efficient charge collection brought about by the excellent in-microsphere contacts and facilitated gel permeation in-between the microspheres. Photoanodes made from size-tunable microspheres have been studied in a gel-electrolyte-based DSSC system, with a commercial nanoparticle film as the reference. The light scattering capability of the microspheres films in the visible spectral region was found to increase significantly when the microsphere size was increased from 200 nm to 400 nm, but much less so from 400 nm to 600 nm. Charge collection for the 200 nm and 400 nm microsphere films turned out to be most efficient of all the four tested photoanode films, due primarily to their longest electron recombination times, facilitated by their optimized pore structures. We have proposed a new mechanism which can explain the microsphere size dependent charge transport properties. Specifically, long and narrow pore channels for the 600 nm microspheres and the nanoparticle films are suggested to hinder gel electrolyte penetration, leading to decrease in their electron recombination times. By judiciously striking a balance between strong light scattering and good charge collection, the 400 nm microsphere based QS-DSSC has achieved the highest efficiency of 6.78%. This work has demonstrated the potential of the mesoporous microspheres in QS-DSSCs and the importance of optimizing the mesoporous microsphere size for attaining the best cell performance. The optimization principle will be of great value for the future development of QS-DSSCs, since the microspheres can be easily produced in large-scale and their hierarchical pore structure is distinct from traditional nanoparticle films, holding a considerable promise to solve the common pore-filling problems in quasi-solid state or solid state DSSCs.

Acknowledgements

This work was supported by the Hong Kong Research Grants Council (RGC) General Research Funds (GRF) no. HKUST 604809 and 605710. We wish to thank Prof. Liduo Wang and Dr. Yantao Shi for supplying the PEO2000000 based gel electrolyte.

Appendix A. Supplementary data

Supplementary data associated with this article can be found, in the online version, at doi:10.1016/j.jpowsour.2011.09.011.

References

[1] D.H. Chen, L. Cao, F.Z. Huang, P. Imperia, Y.B. Cheng, R.A. Caruso, Synthesis of monodisperse mesoporous titania beads with controllable diameter, high surface areas, and variable pore diameters (14–23 nm), J. Am. Chem. Soc. 132 (2010) 4438–4444.

[2] D.H. Chen, F.Z. Huang, Y.B. Cheng, R.A. Caruso, Mesoporous anatase TiO_2 beads with high surface areas and controllable pore sizes: a superior candidate for high-performance dye-sensitized solar cells, Adv. Mater. 21 (2009) 2206–2210.

[3] T.P. Chou, Q.F. Zhang, G.E. Fryxell, G.Z. Cao, Hierarchically structured ZnO film for dye-sensitized solar cells with enhanced energy conversion efficiency, Adv. Mater. 19 (2007) 2588–2591.

[4] F.Z. Huang, D.H. Chen, X.L. Zhang, R.A. Caruso, Y.B. Cheng, Dual-function scattering layer of submicrometer-sized mesoporous TiO_2 beads for high-efficiency dye-sensitized solar cells, Adv. Funct. Mater. 20 (2010) 1301–1305.

[5] K. Park, Q.F. Zhang, B.B. Garcia, X.Y. Zhou, Y.H. Jeong, G.Z. Cao, Effect of an ultrathin TiO_2 layer coated on submicrometer-sized ZnO nanocrystallite aggregates by atomic layer deposition on the performance of dye-sensitized solar cells, Adv. Mater. 22 (2010) 2329–2332.

[6] F. Sauvage, D.H. Chen, P. Comte, F.Z. Huang, L.P. Heiniger, Y.B. Cheng, R.A. Caruso, M. Graetzel, Dye-sensitized solar cells employing a single film of mesoporous TiO_2 beads achieve power conversion efficiencies over 10%, ACS Nano 4 (2010) 4420–4425.

[7] Q.F. Zhang, T.R. Chou, B. Russo, S.A. Jenekhe, G.Z. Cao, Aggregation of ZnO nanocrystallites for high conversion efficiency in dye-sensitized solar cells, Angew. Chem. Int. Ed. 47 (2008) 2402–2406.

[8] Y.J. Kim, M.H. Lee, H.J. Kim, G. Lim, Y.S. Choi, N.G. Park, K. Kim, W.I. Lee, Formation of highly efficient dye-sensitized solar cells by hierarchical pore generation with nanoporous TiO_2 spheres, Adv. Mater. 21 (2009) 1–6.

[9] W.G. Yang, F.R. Wan, Q.W. Chen, J.J. Li, D.S. Xu, Controlling synthesis of well-crystallized mesoporous TiO_2 microspheres with ultrahigh surface area for high-performance dye-sensitized solar cells, J. Mater. Chem. 20 (2010) 2870–2876.

[10] O.K. Varghese, M. Paulose, C.A. Grimes, Long vertically aligned titania nanotubes on transparent conducting oxide for highly efficient solar cells, Nat. Nanotechnol. 4 (2009) 592–597.

[11] K. Zhu, N.R. Neale, A. Miedaner, A.J. Frank, Enhanced charge-collection efficiencies and light scattering in dye-sensitized solar cells using oriented TiO_2 nanotubes arrays, Nano Lett. 7 (2007) 69–74.

[12] K. Zhu, T.B. Vinzant, N.R. Neale, A.J. Frank, Removing structural disorder from oriented TiO_2 nanotube arrays: reducing the dimensionality of transport and recombination in dye-sensitized solar cells, Nano Lett. 7 (2007) 3739–3746.

[13] X.J. Feng, K. Shankar, O.K. Varghese, M. Paulose, T.J. Latempa, C.A. Grimes, Vertically aligned single crystal TiO_2 nanowire arrays grown directly on transparent conducting oxide coated glass: synthesis details and applications, Nano Lett. 8 (2008) 3781–3786.

[14] S.H. Jang, Y.J. Kim, H.J. Kim, W.I. Lee, Low-temperature formation of efficient dye-sensitized electrodes employing nanoporous TiO_2 spheres, Electrochem. Commun. 12 (2010) 1283–1286.

[15] G.K. Mor, J. Basham, M. Paulose, S. Kim, O.K. Varghese, A. Vaish, S. Yoriya, C.A. Grimes, High-efficiency Forster resonance energy transfer in solid-state dye sensitized solar cells, Nano Lett. 10 (2010) 2387–2394.

[16] B. O'Regan, F. Lenzmann, R. Muis, J. Wienke, A solid-state dye-sensitized solar cell fabricated with pressure-treated P25-TiO_2 and CuSCN: analysis of pore filling and *IV* characteristics, Chem. Mater. 14 (2002) 5023–5029.

[17] H.J. Snaith, R. Humphry-Baker, P. Chen, I. Cesar, S.M. Zakeeruddin, M. Graetzel, Charge collection and pore filling in solid-state dye-sensitized solar cells, Nanotechnology 19 (2008) 424003.

[18] F. Falaras, T. Stergiopoulos, D.S. Tsoukleris, Enhanced efficiency in solid-state dye-sensitized solar cells based on fractal nanostructured TiO_2 thin films, Small 4 (2008) 770–776.

[19] S. Nakade, Y. Saito, W. Kubo, T. Kitamura, Y. Wada, S. Yanagida, Influence of TiO_2 nanoparticle size on electron diffusion and recombination in dye-sensitized TiO_2 solar cells, J. Phys. Chem. B 107 (2003) 8607–8611.

[20] N. Kopidakis, E.A. Schiff, N.G. Park, J. van de Lagemaat, A.J. Frank, Ambipolar diffusion of photocarriers in electrolyte-filled, nanoporous TiO_2, J. Phys. Chem. B 104 (2000) 3930–3936.

[21] Q.L. Zhang, L.C. Du, Y.X. Weng, L. Wang, H.Y. Chen, J.Q. Li, Particle-size-dependent distribution of carboxylate adsorption sites on TiO_2 nanoparticle surfaces: insights into the surface modification of nanostructured TiO_2 electrodes, J. Phys. Chem. B 108 (2004) 15077–15083.

[22] V.K.D. LaMer, R.H. Dinegar, Theory, production and mechanism of formation of monodispersed hydrosols, J. Am. Chem. Soc. 72 (1950) 4847–4854.

[23] E.A. Barringer, H.K. Bowen, High-purity, monodisperse TiO_2 powders by hydrolysis of titanium tetraethoxide. 1. Synthesis and physical properties, Langmuir 1 (1985) 414–420.

[24] C.M. Liu, S.H. Yang, Synthesis of angstrom-scale anatase titania atomic wires, ACS Nano 3 (2009) 1025–1031.

[25] K.D.A. Firouzi, L.M. Bull, et al., Cooperative organization of inorganic-surfactant and biomimetic assemblies, Science 267 (1995) 1138–1143.

[26] J. Blanchard, M. In, B. Schaudel, C. Sanchez, Hydrolysis and condensation reactions of transition metal alkoxides: calorimetric study and evaluation of the extent of reaction, Eur. J. Inorg. Chem. (1998) 1115–1127.

[27] X. Peng, J. Wickham, A.P. Alivisatos, Kinetics of II–VI and III–V colloidal semiconductor nanocrystal growth: "focusing" of size distributions, J. Am. Chem. Soc. 120 (1998) 5343–5344.

[28] S. Eiden-Assmann, J. Widoniak, G. Maret, Synthesis and characterization of porous and nonporous monodisperse colloidal TiO_2 particles, Chem. Mater. 16 (2004) 6–11.

[29] Q. Cai, Z.S. Luo, W.Q. Pang, Y.W. Fan, X.H. Chen, F.Z. Cui, Dilute solution routes to various controllable morphologies of MCM-41 silica with a basic medium, Chem. Mater. 13 (2001) 258–263.

[30] B. Jönsson, B. Kronberg, B. Lindman, Surfactants and Polymers in Aqueous Solution, John Wiley & Sons, Chichester, New York, 2003.

[31] C.J. Barbe, F. Arendse, P. Comte, M. Jirousek, F. Lenzmann, V. Shklover, M. Gratzel, Nanocrystalline titanium oxide electrodes for photovoltaic applications, J. Am. Ceram. Soc. 80 (1997) 3157–3171.

[32] B. Smarsly, D. Grosso, T. Brezesinski, N. Pinna, C. Boissiere, M. Antonietti, C. Sanchez, Highly crystalline cubic mesoporous TiO_2 with 10-nm pore diameter made with a new block copolymer template, Chem. Mater. 16 (2004) 2948–2952.

[33] T. Brezesinski, M. Antonietti, B.M. Smarsly, Self-assembled metal oxide bilayer films with "single-crystalline" overlayer mesopore structure, Adv. Mater. 19 (2007) 1074–1078.

[34] Q.F. Zhang, T.P. Chou, B. Russo, S.A. Jenekhe, G. Cao, Polydisperse aggregates of ZnO nanocrystallites: a method for energy-conversion-efficiency enhancement in dye-sensitized solar cells, Adv. Funct. Mater. 18 (2008) 1654–1660.

[35] I.G. Yu, Y.J. Kim, H.J. Kim, C. Lee, W.I. Lee, Size-dependent light-scattering effects of nanoporous TiO_2 spheres in dye-sensitized solar cells, J. Mater. Chem. 21 (2011) 532–538.

[36] Z.S. Wang, H. Kawauchi, T. Kashima, H. Arakawa, Significant influence of TiO_2 photoelectrode morphology on the energy conversion efficiency of N719 dye-sensitized solar cell, Coord. Chem. Rev. 248 (2004) 1381–1389.

[37] Y.T. Shi, C. Zhan, L.D. Wang, B.B. Ma, R. Gao, Y.F. Zhu, Y. Qiu, The electrically conductive function of high-molecular weight poly(ethylene oxide) in polymer gel electrolytes used for dye-sensitized solar cells, Phys. Chem. Chem. Phys. 11 (2009) 4230–4235.

[38] J.H. Wu, Z. Lan, J.M. Lin, M.L. Huang, S.C. Hao, T. Sato, S. Yin, A novel thermosetting gel electrolyte for stable quasi-solid-state dye-sensitized solar cells, Adv. Mater. 19 (2007) 4006–4011.

[39] Z.P. Huo, S.Y. Dai, K.J. Wang, F.T. Kong, C.N. Zhang, X. Pan, X.Q. Fang, Nanocomposite gel electrolyte with large enhanced charge transport properties of an I_3^-/I^- redox couple for quasi-solid-state dye-sensitized solar cells, Sol. Energy Mater. Sol. Cells 91 (2007) 1959–1965.

[40] J.B. Xia, F.Y. Li, C.H. Huang, J. Zhai, L. Jiang, Improved stability quasi-solid-state dye-sensitized solar cell based on polyether framework gel electrolytes, Sol. Energy Mater. Sol. Cells 90 (2006) 944–952.

[41] W. Chen, Y.C. Qiu, Y.C. Zhong, K.S. Wong, S.H. Yang, High-efficiency dye-sensitized solar cells based on the composite photoanocles of SnO_2 nanoparticles/ZnO nanotetrapods, J. Phys. Chem. A 114 (2010) 3127–3138.

[42] K.D. Benkstein, N. Kopidakis, J.V. de Lagemaat, A.J. Frank, Influence of the network geometry on electron transport in nanoparticle networks, Mater. Res. Soc. Symp. Proc. 789 (2004) 325–330.

[43] K.D. Benkstein, N. Kopidakis, J. van de Lagemaat, A.J. Frank, Influence of the percolation network geometry on electron transport in dye-sensitized titanium dioxide solar cells, J. Phys. Chem. B 107 (2003) 7759–7767.

[44] M. Durr, A. Yasuda, G. Nelles, On the origin of increased open circuit voltage of dye-sensitized solar cells using 4-tert-butyl pyridine as additive to the electrolyte, Appl. Phys. Lett. 89 (2006) 061110.

[45] H. Kusama, H. Orita, H. Sugihara, TiO_2 band shift by nitrogen-containing heterocycles in dye-sensitized solar cells: as periodic density functional theory study, Langmuir 24 (2008) 4411–4419.